Subgap modulated photocurrent spectroscopy and its application to the study of the solar cell absorber defect distributions

Z. Djebbour,[1,2] J. Serhan,[1] A. Migan-Dubois,[1] and D. Mencaraglia[1]
[1]*Laboratoire de Génie Electrique de Paris, UMR 8507 CNRS, SUPELEC, Universités UPMC et Paris Sud 11, 11 rue Joliot Curie, Plateau de Moulon, 91190 Gif sur Yvette, France*
[2]*Département de Physique, UVSQ, 45 Av. des Etats Unis, 78035 Versailles CEDEX, France*

(Received 13 November 2009; accepted 21 May 2010; published online 19 August 2010)

In this paper, a theoretical background of subgap modulated photocurrent experiment is presented. It allows the investigation of the density of states (DOS) distribution, directly from the active region of a semiconductor heterojunction device. The junction is illuminated with a modulated subgap light excitation (i.e., light with photon energy lower than the band gap of the active layer). Under specific considerations for the applied reverse bias voltage and the bias-light level, a simple theoretical relation of the imaginary part of the photocurrent versus the modulation angular frequency allows the determination of the energy profile of the gap states. This technique has been successfully applied to a Ga free $Cu(In,Ga)Se_2$ based solar cell to investigate the DOS distribution in the band gap of the absorber. Two distinct defect distributions have been exhibited in the absorber layer of the studied solar cell. © *2010 American Institute of Physics*. [doi:10.1063/1.3456004]

I. INTRODUCTION

Modulated photocurrent spectroscopy (MPCS) is a characterization tool for the determination of the density of states (DOS) and kinetic properties of localized states in semiconductors.[1] Firstly introduced by Niekisch,[2] and extended to a more general case by Oheda,[3] the technique consists in illuminating a voltage biased semiconductor sample, fitted with two coplanar electrodes, the photon energy being higher than the semiconductor band gap and the light intensity being periodically modulated. As a result, electron-hole pairs are generated also with a modulated periodic component. Due to interactions of the whole free carriers (i.e., thermal and photogenerated ones) with band gap states, the resulting modulated photocurrent has an amplitude and a phase shift referred to the photon excitation so that both depend on the gap states characteristics. This technique has been applied to characterize a wide variety of semiconductors such as hydrogenated amorphous silicon,[4] microcrystalline silicon,[5] and $Cu(In,Ga)Se_2$ (CIGS).[6] However, in polycrystalline materials with columnar structure of the grains, the electronic transport, which is parallel to the substrate in coplanar configuration, differs from that in sandwich structure of the solar cell where the transport path of the photogenerated carriers is essentially perpendicular to the substrate. For such materials, it is then interesting to study the modulated photocurrent in sandwich configuration but so far, only few studies have been devoted to this point,[7–11] essentially in the framework of multiple-trapping model and for the case where the light excitation energy is higher than the semiconductor band gap, except works of Abe *et al.*[8] and Mencaraglia *et al.*,[9] where subgap light excitation has been considered.

Contrary to the case of coplanar homogeneous structures where quasi-Fermi levels could be considered flat and abscissa independent, the difficulty to study classic MPCS (i.e., with photon energy larger than the band gap energy) in sandwich structures is that the calculation of the photocurrent, which is controlled by thermal emission and capture processes between defects and extended states, needs more accurate modeling of electrons and holes quasi-Fermi levels, under illumination and reverse biased structure. Indeed, thermal capture processes which are proportional to free carriers concentrations strongly depend on quasi-Fermi levels profile across the structure.

In subgap MPCS (SGMPCS), where the photon energy is lower than the lowest band gap energy of the heterojunction, we can overcome the difficulty of the quasi-Fermi levels abscissa dependence in sandwich structures. Indeed, we will show later in this paper that under given theoretical conditions that can be experimentally fulfilled, the contribution of thermal capture processes to the photocurrent can be neglected.

SGMPCS has been first performed in a-Si:H PIN based solar cells[8] in the framework of the correlated states statistics.[12] In a previous preliminary work,[13] we have given a simple formula relating the DOS distribution of monovalent states to the imaginary part of the subgap ac photocurrent, without developing the theoretical background.

In the present paper, we demonstrate the formula given in our previous work.[13] In Sec. II, we present the calculation from which we deduce the analytical expression of the junction subgap photocurrent, and we show how this expression can lead, under some conditions, to the determination of the $\sigma^{Opt} \times N$ product, where N is the DOS distribution in the band gap of the absorber layer of the junction and σ^{Opt} is the defect optical cross section. In Sec. III, we illustrate these calculations and experimental results by means of simulations that show how the DOS parameters can be deduced from SGMPCS measurements, and finally we conclude in Sec. IV

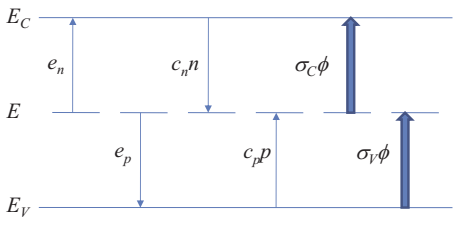

FIG. 1. (Color online) Schematic diagram of the optical transitions and the thermal processes in case of subgap light excitation. Optical transitions between defects levels within the band gap are neglected since their optical cross sections are supposed to be negligible in comparison to those of the main optical transitions involving extended states of higher effective densities of states.

II. THEORY

A. General

In one dimensional model, the continuity equations for electrons and holes can be written as

$$\frac{\partial n}{\partial t} = \frac{1}{q}\frac{\partial}{\partial x} J_n(x,t) + g_n(x,t) - r_n(x,t), \tag{1}$$

$$\frac{\partial p}{\partial t} = -\frac{1}{q}\frac{\partial}{\partial x} J_p(x,t) + g_p(x,t) - r_p(x,t), \tag{2}$$

where $n(p)$ is the density of electrons (holes) in the extended states, $g_n(g_p)$ is the electron (hole) generation rate, $r_n(r_p)$ is the electron (hole) recombination rate, $J_n(J_p)$ is the current density of electrons (holes), and q is the absolute value of the electron charge.

Let us consider a p-type absorber of an n^+p heterostructure, containing monovalent states within the band gap. In order to calculate the carriers generation rates, we consider first a simple case of a monovalent discrete level of density N in the band gap, as it is shown in Fig. 1. Its occupation by electrons is governed by

$$\frac{d(Nf)}{dt} = [-e_n f + c_n n(1-f) + e_p(1-f) - c_p p f + \sigma_V^{Opt}\phi(1-f) - \sigma_C^{Opt}\phi f]N, \tag{3}$$

where $e_n(e_p)$ is the thermal emission rate of electrons (holes) from the trap, $c_n(c_p)$ is the thermal capture coefficient of electrons (holes), $\sigma_C^{Opt}(\sigma_V^{Opt})$ is the defect-to-conduction band (valence band-to-defect) optical cross section, ϕ is a subgap light flux, and f is the occupation function of the trap by electrons under illumination. In this calculation, the photon flux ϕ is supposed to be uniformly absorbed within the absorber region, since the corresponding photon energy is lower than the band gap.

From this discrete level, the net generation rates of electrons and holes can be written as follows:

$$G_n(x,t) = g_n - r_n = \{[e_n + \sigma_C^{Opt}\phi(t)]f(x,t) - c_n n(x)[1-f(x,t)]\}N, \tag{4}$$

$$G_p(x,t) = g_p - r_p = \{[e_p + \sigma_V^{Opt}\phi(t)][1-f(x,t)] - c_p p(x) f(x,t)\}N. \tag{5}$$

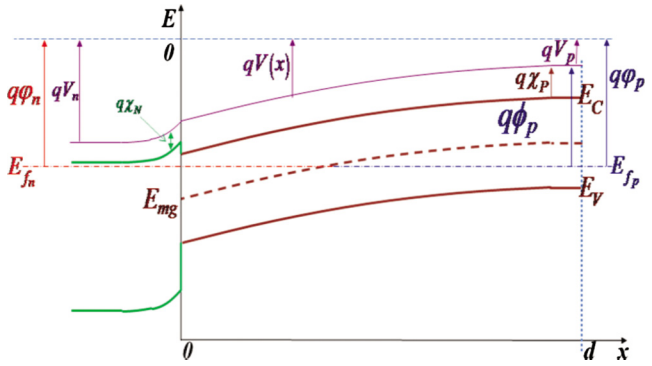

FIG. 2. (Color online) Energy band diagram of an n^+p heterojunction at thermal equilibrium, with the main electrical parameters (φ, the electrochemical potential, V, the electrostatic potential, E_f, the Fermi level, χ, the electronic affinity, and E_{mg}, a level close to midgap: see the text for the definition). All these levels are referred to the zero energy or vacuum level, far from any electrostatic influence.

In case of a continuous defect distribution within the band gap, $N(E)$, these relations become

$$G_n(x,t) = \int_{E_V}^{E_C} \{[e_n(E) + \sigma_C^{Opt}\phi(t)]f(x,t) - c_n n(x,t)[1-f(x,t)]\}N(E)dE, \tag{6}$$

$$G_p(x,t) = \int_{E_V}^{E_C} \{[e_p(E) + \sigma_V^{Opt}\phi(t)][1-f(x,t)] - c_p p(x,t) f(x,t)\}N(E)dE, \tag{7}$$

where $E_C(E_V)$ is the bottom (top) of the conduction (valence) band. In the energy band diagram of Fig. 2, every energy level E is abscissa dependent due to the electrostatic potential spatial variation $V(x)$ as follows:

$$E(x) = E_0 - qV(x), \tag{8}$$

where E_0 is the corresponding energy level, far from any electrostatic potential influence.

The relation between the emission rates and the capture coefficients is given by a classical detailed balance study of the exchange of carriers under thermal equilibrium conditions, between the extended states and a trapping level at energy E, leading to

$$e_n = c_n N_C \exp\left(-\frac{E_C - E}{k_B T}\right); \quad e_p = c_p N_V \exp\left(-\frac{E - E_V}{k_B T}\right), \tag{9}$$

k_B being the Boltzmann constant, T the absolute temperature, and $N_C(N_V)$ the effective densities of states at the bottom (top) of the conduction (valence) band. Under nonequilibrium, which here corresponds to a reverse dc biased n^+p junction illuminated with monochromatic dc and ac photon fluxes, we make the assumption that the capture coefficients c_n and c_p remain unaltered with respect to equilibrium conditions.

B. Small signal regime

For an excitation light with a sinusoidal time variation, to first order, all the time dependent quantities appearing in Eqs. (1)–(7) can be written in the form $F(t)=F_{dc}+F_{ac}\exp(j\omega t)$, ω being the angular frequency. In this case, from Eq. (3), one can easily have the dc and ac small signal regime occupation functions as follows:

$$f_{dc}=\frac{c_n n_{dc}+e_p+\sigma_V^{Opt}\phi_{dc}}{c_n n_{dc}+e_n+c_p p_{dc}+e_p+\sigma_V^{Opt}\phi_{dc}+\sigma_C^{Opt}\phi_{dc}}, \tag{10}$$

$$f_{ac}=\frac{(c_n n_{ac}+\sigma_V^{Opt}\phi_{ac})(1-f_{dc})-(c_p p_{ac}+\sigma_C^{Opt}\phi_{ac})f_{dc}}{A_\omega}, \tag{11}$$

where $A_\omega=c_n n_{dc}+e_n+c_p p_{dc}+e_p+\sigma_V^{Opt}\phi_{dc}+\sigma_C^{Opt}\phi_{dc}+j\omega$.

For a reverse biased and a quasidepleted junction, we assume a time independent high electric field across the illuminated junction, which is a reasonable approximation under small signal ac regime for the bias light. Moreover, we neglect the diffusion contribution to the photocurrent. This latter approximation can be justified by the fact that, under subgap light excitation, free photogenerated carriers are rather uniformly distributed within the quasidepleted junction, and there is no significant gradient of their concentrations. Then, after the separation between dc and ac terms, the modulated part of the continuity Eqs. (1) and (2) can be written

$$\frac{d}{dx}[J_{n_{ac}}(x)]-j\omega\frac{1}{\mu_n E_{dc}(x)}J_{n_{ac}}(x)+qG_{n_{ac}}(x)=0, \tag{12}$$

$$\frac{d}{dx}[J_{p_{ac}}(x)]+j\omega\frac{1}{\mu_p E_{dc}(x)}J_{p_{ac}}(x)-qG_{p_{ac}}(x)=0, \tag{13}$$

where $\mu_n(\mu_p)$ is the electron (hole) mobility.

From Eqs. (6) and (7), the modulated part of the ac generation rates appearing in the above equations take the form:

$$G_{n_{ac}}(x)=\int_{E_V}^{E_C}\left[\left\{\frac{(e_n+\sigma_C^{Opt}\phi_{dc}+c_n n_{dc})(c_n n_{ac}+\sigma_V^{Opt}\phi_{ac})}{A_\omega}-c_n n_{ac}\right\}(1-f_{dc})+\left\{\sigma_C^{Opt}\phi_{ac}-\frac{(e_n+\sigma_C^{Opt}\phi_{dc}+c_n n_{dc})(c_p p_{ac}+\sigma_C^{Opt}\phi_{ac})}{A_\omega}\right\}f_{dc}\right]N(E)dE, \tag{14}$$

$$G_{p_{ac}}(x)=\int_{E_V}^{E_C}\left[\left\{\frac{(e_p+\sigma_V^{Opt}\phi_{dc}+c_p p_{dc})(c_p p_{ac}+\sigma_C^{Opt}\phi_{ac})}{A_\omega}-c_p p_{ac}\right\}f_{dc}+\left\{\sigma_V^{Opt}\phi_{ac}-\frac{(e_p+\sigma_V^{Opt}\phi_{dc}+c_p p_{dc})(c_n n_{ac}+\sigma_V^{Opt}\phi_{ac})}{A_\omega}\right\}(1-f_{dc})\right]N(E)dE. \tag{15}$$

C. Spatial subregions of the junction absorber layer

In order to get simplified expressions of the generation rates given above, all the dc thermal frequencies, included in Eqs. (10), (14), and (15), which are energy level dependent and/or position dependent, must be compared with each other. For this goal, in the case of a reverse biased heterojunction, we use a simplified model for the quasi-Fermi levels[14] as indicated in Fig. 3, where the quasi-Fermi level of electrons E_{f_n} is aligned with the Fermi level of the n^+ region and remains flat until it crosses E_{mg} [a level defined in Eq. (18)], and that of holes E_{f_p} is aligned with the bulk Fermi level of the p region and remains flat until it crosses the level E_{mg}.

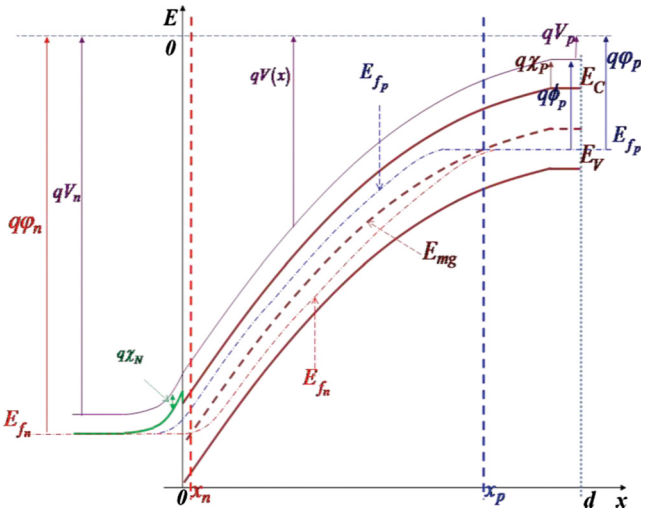

FIG. 3. (Color online) Energy band diagram of an n^+p heterojunction under reverse bias conditions, with the model of quasi-Fermi levels of electrons and holes as indicated in the text. The p region is divided into three spatial subregions, delimited by x_n and x_p abscissa given in the text.

In this case, the p region of the junction can be divided into three spatial subregions, delimited by x_n and x_p abscissa given by

$$E_{mg}(x_n)=E_{mg_0}-qV(x_n)=E_{f_n}, \tag{16}$$

$$E_{mg}(x_p)=E_{mg_0}-qV(x_p)=E_{f_p}, \tag{17}$$

E_{mg} being the energy level where emission frequencies of electrons and holes are equal:

$$e_n(E_{mg})=e_p(E_{mg}). \tag{18}$$

Assuming the same order of magnitude for the pre-exponential factors of electron and hole emission frequencies, [cf. Eq. (9)], one can see that E_{mg} is close to midgap.

Results of comparison of thermal emission and capture frequencies in both the upper and the lower half of midgap of the three subregions of the p layer are given in the Appendix, with the corresponding simplified dc occupation functions (cf. Table V of the Appendix).

It is noteworthy that the central subregion (i.e., $x_n < x < x_p$) extends with increasing reverse bias, and dominates the region p at the expense of extreme regions when the junction is completely depleted (i.e., $x_n \to 0$ and $x_p \to d$, where d is the thickness of the p region). In this case, only net generation rates in this central subregion have to be considered in the photocurrent calculation. Let us consider in the following two special cases of defects type: a donorlike defect [i.e., defect with distribution $N_D(E)$ peaked at $E_D > E_{mg}$] and an acceptorlike defect [i.e., defect with distribution $N_A(E)$ peaked at $E_A < E_{mg}$].

D. Case of donorlike defect

In this case, the major contribution to the net generation rate comes from defects with energy levels located at the upper half of midgap (i.e., $E > E_{mg}$). According to thermal emission and capture frequencies comparison within the central subregion (i.e., $x_n < x < x_p$) given in the Appendix (i.e., $e_n \gg c_n n_{dc}$, $e_n \gg c_p p_{dc}$, and $e_n \gg e_p$), the generation rates of Eqs. (14) and (15) become

$$G_{n_{ac}} \approx \int_{E_V}^{E_C} \left[\left\{ \frac{(e_n + \sigma_C^{Opt}\phi_{dc})(c_n n_{ac} + \sigma_V^{Opt}\phi_{ac})}{e_n + \sigma_V^{Opt}\phi_{dc} + \sigma_c^{Opt}\phi_{dc} + j\omega} - c_n n_{ac} \right\} \frac{e_n + \sigma_C^{Opt}\phi_{dc}}{e_n + \sigma_V^{Opt}\phi_{dc} + \sigma_C^{Opt}\phi_{dc}} + \left\{ \sigma_C^{Opt}\phi_{ac} - \frac{(e_n + \sigma_C^{Opt}\phi_{dc})(c_p p_{ac} + \sigma_C^{Opt}\phi_{ac})}{e_n + \sigma_V^{Opt}\phi_{dc} + \sigma_C^{Opt}\phi_{dc} + j\omega} \right\} \frac{c_n n_{dc} + e_p + \sigma_V^{Opt}\phi_{dc}}{e_n + \sigma_V^{Opt}\phi_{dc} + \sigma_C^{Opt}\phi_{dc}} \right] N_D(E)dE, \tag{19}$$

$$G_{p_{ac}} \approx \int_{E_V}^{E_C} \left[\left\{ \frac{(e_p + \sigma_V^{Opt}\phi_{dc} + c_p p_{dc})(c_p p_{ac} + \sigma_C^{Opt}\phi_{ac})}{e_n + \sigma_V^{Opt}\phi_{dc} + \sigma_C^{Opt}\phi_{dc} + j\omega} - c_p p_{ac} \right\} \frac{c_n n_{dc} + e_p + \sigma_V^{Opt}\phi_{dc}}{e_n + \sigma_V^{Opt}\phi_{dc} + \sigma_C^{Opt}\phi_{dc}} + \left\{ \sigma_V^{Opt}\phi_{ac} - \frac{(e_p + \sigma_V^{Opt}\phi_{dc} + c_p p_{dc})(c_n n_{ac} + \sigma_V^{Opt}\phi_{ac})}{e_n + \sigma_V^{Opt}\phi_{dc} + \sigma_C^{Opt}\phi_{dc} + j\omega} \right\} \frac{e_n + \sigma_C^{Opt}\phi_{dc}}{e_n + \sigma_V^{Opt}\phi_{dc} + \sigma_C^{Opt}\phi_{dc}} \right] N_D(E)dE. \tag{20}$$

Let us now introduce a new level E_{ϕ_n}, as follows:

$$e_n(E_{\phi_n}) = \sigma_C^{Opt}\phi_{dc} + \sigma_V^{Opt}\phi_{dc}. \tag{21}$$

The level position of E_{ϕ_n}, can be tuned by the dc photon flux intensity and kept far away below the donorlike peak level E_D so that the main part of the donorlike defect distribution $N_D(E)$ lies above E_{ϕ_n} (this assumption will be discussed quantitatively in Sec. III). In this case, for this main part of $N_D(E)$, in Eqs. (19) and (20) we can neglect dc optical transition frequencies compared to the electrons thermal emission frequency because, as $E > E_{\phi_n}$, then from Eq. (9) we have $e_n(E) > e_n(E_{\phi_n}) = \sigma_C^{Opt}\phi_{dc} + \sigma_V^{Opt}\phi_{dc}$. Then, the generation rates can be simplified as

$$G_{n_{ac}}(x) \approx \int_{E_V}^{E_C} \left[\left\{ \frac{e_n(c_n n_{ac} + \sigma_V^{Opt}\phi_{ac})}{e_n + j\omega} - c_n n_{ac} \right\} + \left\{ \sigma_C^{Opt}\phi_{ac} - \frac{e_n(c_p p_{ac} + \sigma_C^{Opt}\phi_{ac})}{e_n + j\omega} \right\} \frac{c_n n_{dc} + e_p + \sigma_V^{Opt}\phi_{dc}}{e_n} \right] N_D(E)dE, \tag{22}$$

$$G_{P_{ac}}(x) \approx \int_{E_V}^{E_C} \left[\left\{ \frac{(e_p + \sigma_V^{Opt}\phi_{dc} + c_p p_{dc})(c_p p_{ac} + \sigma_C^{Opt}\phi_{ac})}{e_n + j\omega} - c_p p_{ac} \right\} \frac{c_n n_{dc} + e_p + \sigma_V^{Opt}\phi_{dc}}{e_n} + \left\{ \sigma_V^{Opt}\phi_{ac} - \frac{(e_p + \sigma_V^{Opt}\phi_{dc} + c_p p_{dc})(c_n n_{ac} + \sigma_V^{Opt}\phi_{ac})}{e_n + j\omega} \right\} \right] N_D(E)dE. \tag{23}$$

The above expressions can be further simplified for the same reasons ($e_n \gg c_n n_{dc}$, $e_n \gg c_p p_{dc}$, $e_n \gg e_p$ and $e_n \gg \sigma_V^{Opt}\phi_{dc}$), since within the presently considered central subregion (i.e., $x_n < x < x_p$) we have

$$\frac{c_n n_{dc} + e_p + \sigma_V^{Opt}\phi_{dc}}{e_n} \ll 1, \tag{24}$$

and

$$\left|\frac{e_p+\sigma_V^{Opt}\phi_{\rm dc}+c_p p_{\rm dc}}{e_n+j\omega}\right| \ll 1. \tag{25}$$

Then, the net ac generation rates become

$$G_{n_{\rm ac}}(x) \approx \int_{E_V}^{E_C}\left[\frac{e_n(c_n n_{\rm ac}+\sigma_V^{Opt}\phi_{\rm ac})}{e_n+j\omega}-c_n n_{\rm ac}\right]N_D(E)dE, \tag{26}$$

$$G_{p_{\rm ac}}(x) \approx \int_{E_V}^{E_C}\sigma_V^{Opt}\phi_{\rm ac}N_D(E)dE. \tag{27}$$

Note that the simplified ac generation rate of holes is then position independent. This is not the case of the generation rate of electrons. It could be the case if the angular frequency of the light modulation ω is smaller than ω_{n_0} where ω_{n_0} is given by

$$\omega_{n_0}=\frac{e_n\sigma_V^{Opt}\phi_{\rm ac}}{c_n n_{\rm ac}}. \tag{28}$$

This condition is easily achievable since, under small signal regime, $c_n n_{\rm ac}$ is very small compared to $c_n n_{\rm dc}$ which is negligible, compared to the electron thermal emission frequency (cf., Table III of the Appendix), so that the angular frequency ω_{n_0} can be rather large.

We assume this condition experimentally fulfilled. Then, the net generation rate of electrons becomes

$$G_{n_{\rm ac}} \approx \int_{E_V}^{E_C}\frac{e_n\sigma_V^{Opt}\phi_{\rm ac}}{e_n+j\omega}N_D(E)dE. \tag{29}$$

In these conditions, it is now easy to integrate Eqs. (12) and (13), assuming a uniform dc electric field

$$J_{n_{\rm ac}}(x)=K_n e^{j\omega(x/\mu_n E_{\rm dc})}+\frac{q\mu_n E_{\rm dc}G_{n_{\rm ac}}}{j\omega}, \tag{30}$$

$$J_{p_{\rm ac}}(x)=K_p e^{-j\omega(x/\mu_p E_{\rm dc})}+\frac{q\mu_p E_{\rm dc}G_{p_{\rm ac}}}{j\omega}, \tag{31}$$

where K_n and K_p are integration constants determined from the boundaries conditions.

In our case, taking into account the reverse biased operating conditions, we assume a large enough electric field permitting to write that the ac photogenerated holes (electrons, respectively) density can be neglected at the front (back, respectively) interface. In this case, we can write that $J_{p_{\rm ac}}(0)\approx 0$ and $J_{n_{\rm ac}}(d)\approx 0$, so that Eqs. (30) and (31) become

$$J_{n_{\rm ac}}(x)=\frac{q\mu_n E_{\rm dc}G_{n_{\rm ac}}}{j\omega}[1-e^{j\omega(x-d)/\mu_n E_{\rm dc}}], \tag{32}$$

$$J_{p_{\rm ac}}(x)=\frac{q\mu_p E_{\rm dc}G_{p_{\rm ac}}}{j\omega}[1-e^{-j\omega(x/\mu_p E_{\rm dc})}]. \tag{33}$$

Assuming that the modulation period is greater than the mean transit time of both electrons and holes, t_n and t_p given by

$$t_n=\frac{d}{\mu_n E_{\rm dc}} \tag{34}$$

and

$$t_p=\frac{d}{\mu_p E_{\rm dc}}, \tag{35}$$

it is then possible to use a Taylor series first order development of Eqs. (32) and (33)

$$J_{n_{\rm ac}}(x)\approx\frac{q\mu_n E_{\rm dc}G_{n_{\rm ac}}}{j\omega}\left[1-\left(1+\frac{j\omega(x-d)}{\mu_n E_{\rm dc}}\right)\right]=qG_{n_{\rm ac}}(d-x), \tag{36}$$

$$J_{p_{\rm ac}}(x)\approx\frac{q\mu_p E_{\rm dc}G_{p_{\rm ac}}}{j\omega}\left[1-\left(1-\frac{j\omega x}{\mu_p E_{\rm dc}}\right)\right]=qG_{p_{\rm ac}}x. \tag{37}$$

The total ac current can then be written as

$$J_{\rm ac}(x)=J_{n_{\rm ac}}(x)+J_{p_{\rm ac}}(x)\approx q(d-x)G_{n_{\rm ac}}+qxG_{P_{\rm ac}}. \tag{38}$$

Thus, following Longeaud *et al.*,[15] the external ac current is given by

$$I_{\rm ac}\approx\frac{S}{d}\int_0^d[J_{n_{\rm ac}}(x)+J_{p_{\rm ac}}(x)]dx\approx\frac{Sq(G_{n_{\rm ac}}+G_{p_{\rm ac}})d}{2}\approx\frac{Sqd}{2}\int_{E_V}^{E_C}\left[\frac{e_n\sigma_V^{Opt}\phi_{\rm ac}}{e_n+j\omega}+\sigma_V^{Opt}\phi_{\rm ac}\right]N_D(E)dE, \tag{39}$$

where S is the surface area of the junction.

From Eq. (39), the imaginary part of the ac photocurrent is given by

$$\Im m[I_{\rm ac}]\approx\frac{-Sqd}{2}\int_{E_V}^{E_C}\frac{\omega e_n}{e_n^2+\omega^2}\sigma_V^{Opt}\phi_{\rm ac}N_D(E)dE, \tag{40}$$

where

$$\delta_n(E)=\frac{\omega e_n(E)}{e_n^2(E)+\omega^2} \tag{41}$$

is a sharp peaked function centered at E_{ω_n} defined by $e_n(E_{\omega_n})=\omega$. This function can be approximated by Dirac δ function[3,16] so that

$$\Im m[I_{\rm ac}]\approx\frac{-Sqd\pi k_B T}{4}\sigma_V^{Opt}\phi_{\rm ac}N_D(E_{\omega_n})=A(T)\times\sigma_V^{Opt}N_D(E_{\omega_n}). \tag{42}$$

Following Eq. (9), E_{ω_n} is given by

$$\Delta E_{\omega_n}=E_C-E_{\omega_n}=k_B T\ln\left(\frac{c_n N_C}{\omega}\right)=k_B T\ln\left(\frac{\xi_{n_0}T^2}{\omega}\right), \tag{43}$$

where T^2 has been introduced to exhibit explicitly the usual dependence with temperature of the conduction band effective DOS and of the electron thermal velocity included in the thermal capture coefficient.

TABLE I. Simulation parameters used to test the validity of the pseudo-Dirac approximation. Results of the simulation are plotted in Fig. 4.

	Gaussian parameters							
	N_0 (cm^{-3} eV^{-1})	σ_0 (meV)	E_C-E_0 (meV)	Absorber thickness (cm)	ac photon flux (ph cm^{-2} s^{-1})	Surface area (cm^2)	Optical cross section (cm^2)	ξ_0 (s^{-1} K^{-2})
Defect 1	3×10^{16}	35	100	1.5×10^{-4}	7.5×10^{11}	0.47	5×10^{-13}	175

These two last equations show that by measuring the imaginary part of the ac photocurrent of a reverse biased junction under small signal regime, one can perform the spectroscopy of the DOS. Indeed, at given angular frequency ω and temperature T, the major contribution to the imaginary part of the ac photocurrent is due to a defect located at an energy level E_{ω_n} given by Eq. (43). It is then easy to reconstruct the defect distribution by varying ω and T.

It is also possible to do the spectroscopy of the DOS from the real part of the ac photocurrent, as it is described below.

From Eq. (39), the real part of the ac photocurrent is given by

$$\Re e[I_{\rm ac}] \approx \frac{Sqd}{2}\int_{E_V}^{E_C}\left[\frac{e_n^2}{e_n^2+\omega^2}+1\right]\sigma_V^{Opt}\phi_{\rm ac}N_D(E)dE, \tag{44}$$

which becomes

$$\Re e[I_{\rm ac}] \approx \frac{Sqd}{2}\int_{E_V}^{E_C}\left[\frac{1}{1+e^{\frac{2(E-E_{\omega_n})}{k_BT}}}+1\right]\sigma_V^{Opt}\phi_{\rm ac}N_D(E)dE$$
$$= \frac{Sqd}{2}\int_{E_V}^{E_C}[f_{\omega_n}(E)+1]\sigma_V^{Opt}\phi_{\rm ac}N_D(E)dE \tag{45}$$

by replacing ω by $e_n(E_{\omega_n})$ and $e_n(E)$ with its expression given in Eq. (9).

$f_{\omega_n}(E)$ looks like the Fermi–Dirac function where the Fermi level is replaced by E_{ω_n} and k_BT by $k_BT/2$. It is then easy to show that

$$\frac{\partial f_{\omega_n}(E)}{\partial \ln \omega} = \frac{\partial f_{\omega_n}(E)}{\partial E_{\omega_n}}\cdot\frac{\partial E_{\omega_n}}{\partial \ln \omega} = -k_BT\cdot\delta(E-E_{\omega_n}). \tag{46}$$

Thus, by differentiating Eq. (45) with respect to $\ln\omega$, one can easily find

$$\frac{\partial \Re e[I_{\rm ac}]}{\partial \ln \omega} \approx \frac{-Sqd}{2}\int_{E_V}^{E_C}k_BT\cdot\delta(E-E_{\omega_n})\sigma_V^{Opt}\phi_{\rm ac}N_D(E)dE$$
$$\approx \frac{-Sqdk_BT}{2}\sigma_V^{Opt}\phi_{\rm ac}N_D(E_{\omega_n}). \tag{47}$$

The above expression (47) is similar to that found by Abe *et al.*,[8] but in the framework of correlated states statistics.[12] One can then have access to DOS spectroscopy also from the real part of the photocurrent from Eq. (47) but using instead Eq. (42) avoids the use of a numerical differentiation which can introduce additional numerical noise to the data treatment.

E. Case of acceptorlike defect

Following the same approach as in Sec. II D, it can be shown that the contribution of the acceptorlike defects to the photocurrent can be written

$$\Im m[I_{\rm ac}] \approx \frac{-Sqd\pi k_BT}{4}\sigma_C^{Opt}\phi_{\rm ac}N_A(E_{\omega_p}), \tag{48}$$

where E_{ω_p} is such that $e_p(E_{\omega_p})=\omega$ and is given by

$$\Delta E_{\omega_p} = E_{\omega_p}-E_V = k_BT\ln\left(\frac{c_pN_V}{\omega}\right) = k_BT\ln\left(\frac{\xi_{p_0}T^2}{\omega}\right). \tag{49}$$

III. EXPERIMENTAL RESULTS AND DISCUSSION

In order to validate our model, we have compared MATLAB simulations with experimental results.

First of all, we calculate the imaginary part of the ac photocurrent, when a single donorlike Gaussian defect is considered. The Gaussian distribution introduced in Eq. (40) is given as follows:

$$N_D(E) = N_0\exp\left[-\frac{(E-E_0)^2}{2\sigma_0^2}\right], \tag{50}$$

where E_0, N_0, and σ_0 represent the peak energetic position, the peak DOS and the standard deviation, respectively.

Using the numerical values indicated in Table I, we have then compared the entire expression, given by Eq. (40), with the pseudo-Dirac approximation, Eq. (42). The calculated imaginary part of the photocurrent using Eq. (40) is plotted versus the angular frequency in Fig. 4(a), for six temperatures. Figure 4(b) shows that the corresponding Arrhenius plot of the angular frequency position, divided by T^2, of the maximum of each curve, is thermally activated with an activation energy E_a=98 meV and a pre-exponential factor equal to 128 s^{-1} K^{-2}. Interpreting this pre-exponential factor as the ξ_{n_0} parameter appearing in Eq. (43), we can now plot versus the energy given by the same equation, the imaginary part of the photocurrent divided by $A(T)$ appearing in Eq. (42). The result is shown in Fig. 4(c) and compared with the introduced Gaussian distribution for the calculation of the photocurrent. We note from this latter figure that the reconstructed $\sigma^{Opt}\times N$ product and the introduced one $\sigma^{Opt}\times N_{int}$, are in very good agreement, and we have checked that, as expected, this agreement is as better as the standard deviation is larger.

More precisely, we have observed that the energetic resolution of both Eqs. (42) and (47) is poor for DOS Gaussian distributions with a standard deviation lower than 2 k_BT.

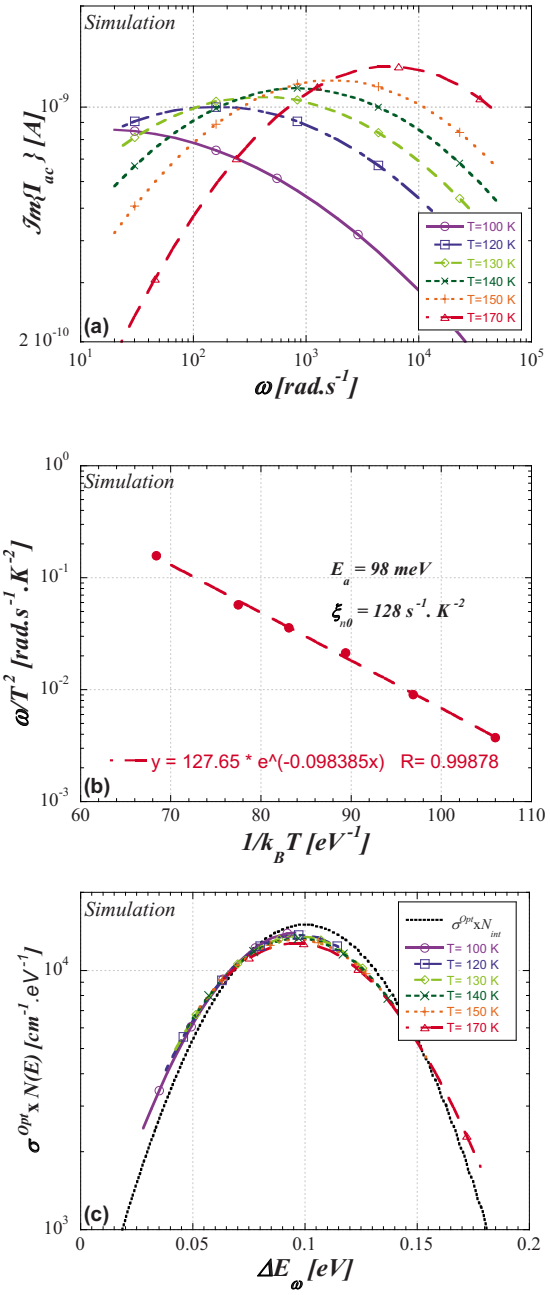

FIG. 4. (Color online) Calculated imaginary part of the photocurrent from Eq. (40) vs angular frequency, using a Gaussian shape of the DOS (a), the deduced Arrhenius plot of the quantity ω_0/T^2, ω_0(T) being the angular frequency corresponding to the photocurrent maximum for a given temperature T (b), and the reconstruction of the $\sigma^{Opt} \times N$ product vs the energy ΔE_ω, using Eq. (43) (c), at various temperatures. The comparison with the pseudo-Dirac approximation [i.e., Eq. (42)] using the introduced Gaussian N_{int}, is added.

Figure 5 shows an example of the imaginary part of the experimental ac photocurrent of a CIGS/CdS based solar cell, illuminated with a monochromatic subgap light excitation of small photon flux. This solar cell belongs to a series of CIGS based solar cells with different gallium content, and with the same buffer layer (CdS). The CIGS thin films have been grown by the coevaporation of elemental Cu, In, Ga, and Se following the three-stage process.[17] The Ga content of the studied solar cell here is 0%.

During the measurement of the photocurrent of this solar

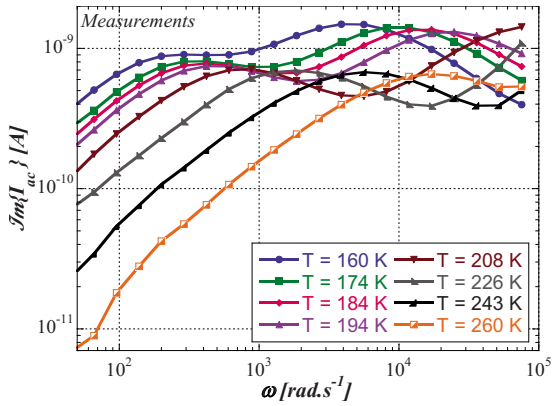

FIG. 5. (Color online) An example of measured imaginary part of the subgap ac photocurrent vs angular frequency, at different temperatures, in case of Ga free CIGS/CdS based solar cell.

cell, temperature varies from 160 to 260 K and the frequency ranges from 5 Hz to 12 kHz. The monochromatic light of wavelength $\lambda = 1304 \pm 30$ nm (which allows subgap excitation for an absorber of about 1 eV of the band gap energy), has a dc photon flux of 2×10^{12} ph cm^{-2}s^{-1} and an ac photon flux of 7.5×10^{11} ph cm^{-2} s^{-1}.

An Arrhenius plot of the quantities ω_0/T^2, where ω_0 represents the abscissa of the relative photocurrent maxima in Fig. 5, is given in Fig. 6, and shows that in a given temperature range, the photocurrent is thermally activated and two activation energies are exhibited. Referring to the above discussion of the simulation results at the beginning of this section, we then interpret these two activation energies as the peak positions of two distinct defect distributions located at 93 and 248 meV, the pre-exponential factors divided by T^2 of the corresponding emission frequencies, ξ_{01} and ξ_{02}, being, respectively, equal to 176 and 16 000 s^{-1} K^{-2}.

We note in Fig. 6 that for the deepest distribution, peaked at 248 meV, the lack of thermal activation behavior below a temperature around 200 K could be due to a too small contribution, as the temperature decreases, of the thermal emission process compared to the optical transitions.

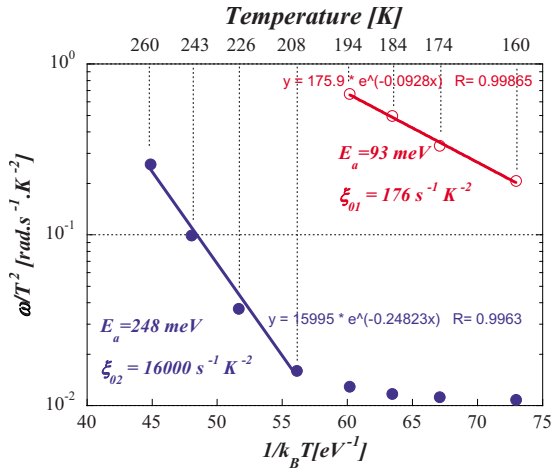

FIG. 6. (Color online) Arrhenius plot of the quantities ω_0/T^2 extracted from Fig. 5 as mentioned in the text. Two activation energies corresponding to the peak energetic positions of two distinct defect distributions have been extracted.

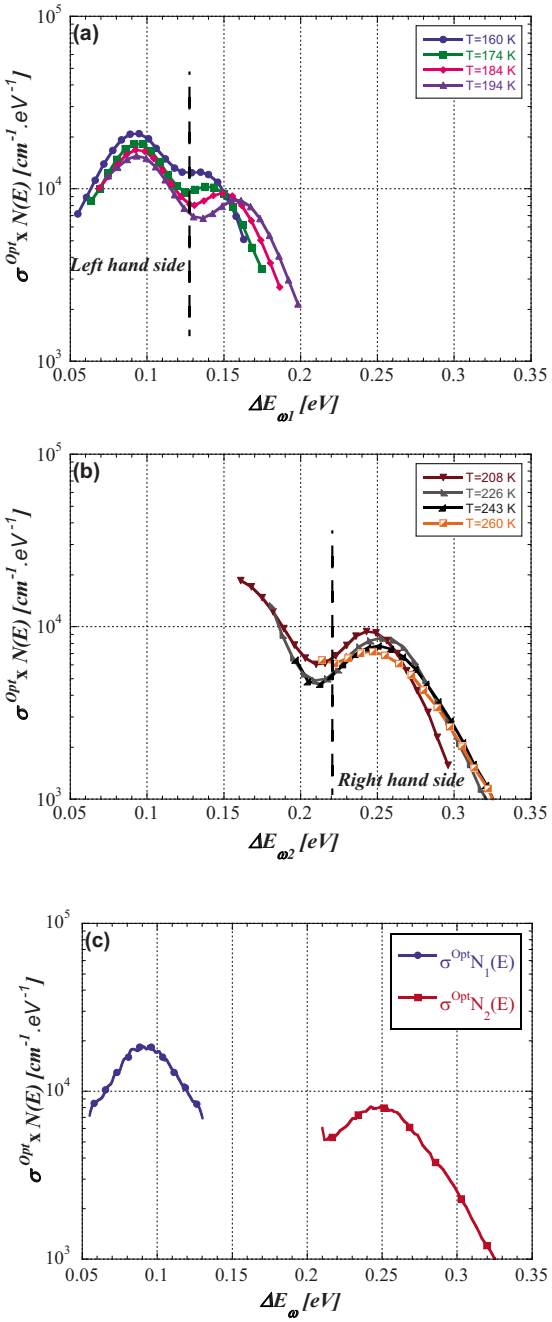

FIG. 7. (Color online) Reconstructed $\sigma^{Opt} \times N$ product deduced from photocurrent measurements vs frequency and temperature, and plotted vs the energy $\Delta E_{\omega 1}$ (a), and $\Delta E_{\omega 2}$ (b). The mean curve of the quasisuperimposed products [left hand side in (a) and right hand side in (b)] is plotted vs ΔE_{ω} in (c). See text for details of this construction.

Following Eqs. (42) and (43), from the measured photocurrent versus ω, reported in Fig. 5, one can try to get the $\sigma^{Opt} \times N$ product versus the energy ΔE_{ω}, as we have shown with the simulation for a single defect distribution at the beginning of this section. However, if we want to apply the same method to the result of Fig. 5, the problem is now that we are dealing with two energy scales associated to the two different emission frequencies of the two distributions. Consequently, the strategy is then first to plot the photocurrent as a function of ΔE_{ω}, given either by one energy scale or by the other, as this has been done in Figs. 7(a) and 7(b) and then to keep only the parts of the distributions where all the curves obtained at different temperatures are superimposed because this means that the used energy scale was the appropriate one. Figure 7 then shows that in Fig. 7(a) (respectively, Fig. 7(b)), only the left hand side (respectively right hand side) of the distribution, as indicated by the vertical dashed line, has to be considered. The result is summarized in Fig. 7(c) where the mean curve of the superimposed parts that have been kept is represented for the two defect distributions. Note that both reconstructed DOS distributions have been plotted here with the same energy axis for convenience but, depending on the type of defect, ΔE_{ω} will represent either $E_c - E$ for a donorlike defect or $E - E_v$ for an acceptorlike (we will see in the following that this information cannot be derived from the SGMPCS technique only).

In order to assess the validity of this experimental procedure in the case of two distinct defect distributions, we have used our MATLAB simulation to calculate the photocurrent and then to reconstruct the introduced DOS distribution as was done for the data treatment of the experimental photocurrent of Fig. 5. For this purpose, we have used two Gaussian distributions representing in a first step two distinct donorlike defects, located at 94 and 250 meV from the conduction band. All the parameters of these Gaussian distributions used to calculate the theoretical simulated photocurrent from Eq. (40) have been chosen of the same order of magnitude as the experimentally derived ones and the other needed parameters are known from our experimental conditions or from the sample geometry. All these parameters are summarized in Table II. The corresponding results are shown on one hand in Figs. 8(a) and 8(b), respectively, for the simulated photocurrent and extracted parameters of the thermal emission frequencies corresponding to the two defect distributions and on the other hand in Figs. 8(c) and 8(d) for the reconstructed DOS. These two last Figures show the DOS reconstruction performed with Eq. (42) using either one or the other energy scale provided by Eq. (43) with the two derived pre-exponential factors ξ_{01} and ξ_{02}, of the thermal emission frequencies in Fig. 8(b). We can note that these prefactor values and the activation energies are very close to those associated to the thermal emission frequencies of the two peaks defect distributions introduced in Table II for the simulation purpose. Figures 8(c) and 8(d) confirm that when

TABLE II. Simulation parameters used to reconstruct the experimental DOS of Fig. 7. Results of the simulation are plotted in Fig. 8.

	Gaussian parameters							
	N_0 (cm^{-3} eV^{-1})	σ_0 (meV)	$E_C - E_0$ (meV)	Absorber thickness (cm)	ac photon flux (ph cm^{-2} s^{-1})	Surface area (cm^2)	Optical cross section (cm^2)	ξ_0 (s^{-1} K^{-2})
Defect 1	3×10^{16}	18	94	1.5×10^{-4}	7.5×10^{11}	0.47	5×10^{-13}	175
Defect 2	2×10^{16}	35	250	1.5×10^{-4}	7.5×10^{11}	0.47	5×10^{-13}	16013

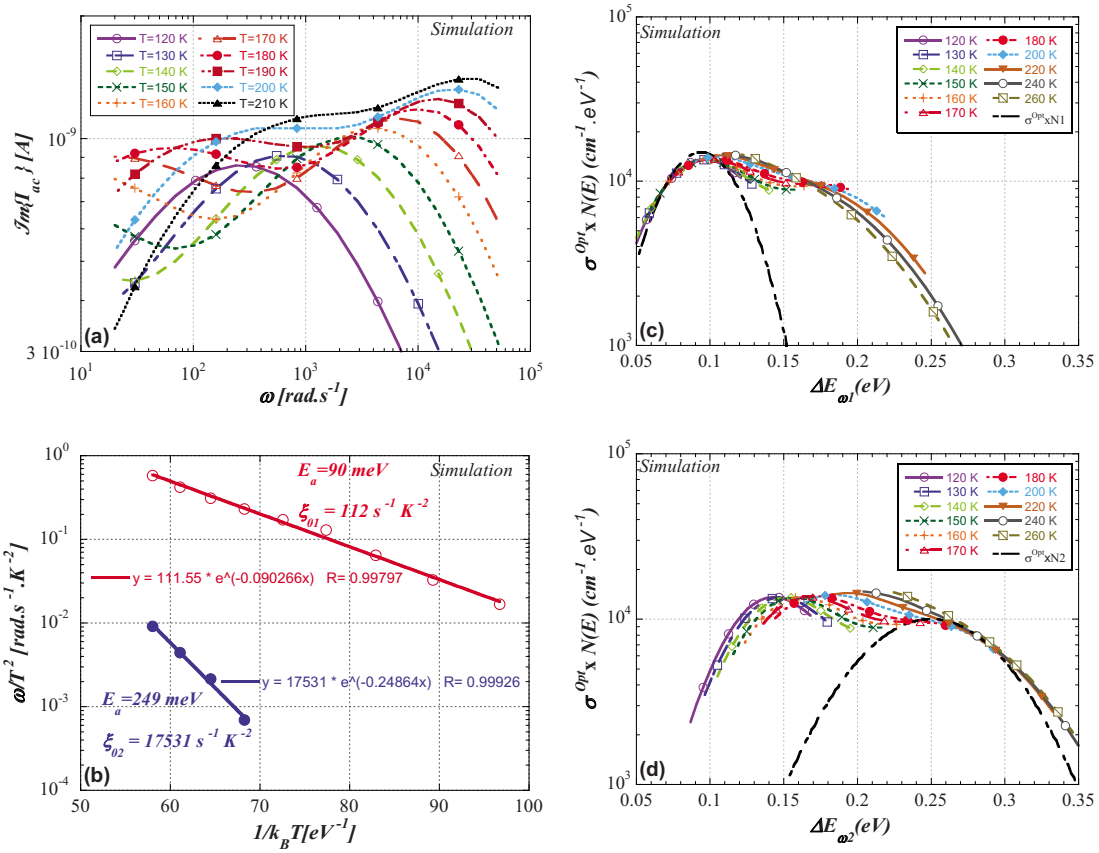

FIG. 8. (Color online) Simulated imaginary part of ac photocurrent vs frequency and temperature, with two distinct Gaussian DOS defect distributions (a), the deduced Arrhenius plot (b) and the derived $\sigma^{Opt} \times N$ product vs the energy $\Delta E_{\omega 1}$ (c), and $\Delta E_{\omega 2}$ (d). The parameters used in this simulation are summarized in Table II. The introduced defect DOS distributions, multiplied with the optical cross section, are plotted separately in (c) for the shallow defect and in (d) for the deepest one.

the reconstructed DOS distributions calculated at different temperatures are well superimposed in a certain energy range, the corresponding superimposed parts are representative of the Gaussian distributions introduced in the simulation. This method permits then to determine which energy scale corresponds to one or the other distribution when we are dealing with more than a single type of defect, defining then the respective thermal emission frequency of each distribution.

Note that the agreement between the reconstructed part of the DOS distributions in Figs. 8(c) and 8(d) with the introduced ones could have been even better if the Gaussian standard deviations values were chosen a little bit larger for the simulation. Indeed, we have taken here 18 and 35 meV for the shallow and deep defect respectively, which are slightly less than the 2 k_BT energy range (20–34 meV) corresponding to the temperature range used to reconstruct the DOS. We can see that the standard deviations values used in the simulation were rather stringent and could have been chosen closer to the experimental values deduced from Fig. 7(c) which are respectively equal to 25 and 50 meV, but we wanted to show here that even with rather stringent conditions, the DOS can be reconstructed satisfactorily.

In a second step, we have also tested, on one hand, two distinct acceptorlike defects, and on the other hand, a donorlike defect, using Eq. (42), with an acceptorlike defect, using Eq. (48). We have then observed that all these different simulated results show the same good agreement with the experimental result. This is not surprising as Eqs. (42) and (48) on one hand, and Eqs. (43) and (49) on the other hand are the same if we exchange the parameters related to electrons and donor levels with those related to holes and acceptor levels. This means that the SGMPCS technique, like admittance spectroscopy[18] (AS), is not able to distinguish between acceptorlike and donorlike defects. In fact, such defect identification needs correlation of SGMPCS and AS analysis with that of another defect spectroscopy technique, such as DLTS for instance.

To conclude the above discussion on the ability of our analytical model to reconstruct the DOS distribution from the imaginary part of the ac photocurrent, we can also point that the interest of the simulation was twofold: (i) firstly, it has permitted to check the validity of the use of the Dirac δ function approximation to derive the simple analytical expression of Eq. (42) from the integral expression of the photocurrent presented in Eq. (40), which is a rather classical approach when dealing with occupation functions of the gap states by free carriers, and (ii) the second even more important point is the demonstrated ability of Eq. (42) to nicely reproduce the main evolutions of the measured photocurrent with temperature and frequency. This last point is a good assessment of our developed analysis of the SGMPCS technique, but one has to keep in mind that the experimental

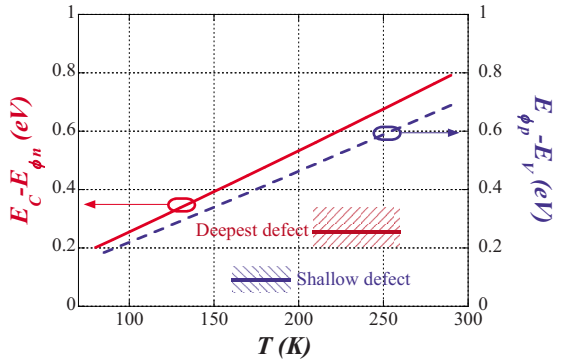

FIG. 9. (Color online) Energy position of the energy level E_{ϕ_n}, introduced in Eq. (21) for donorlike defects, and its equivalent, E_{ϕ_p}, corresponding to acceptorlike defects, in the case of CIGS. The peak energy position (horizontal lines), the energy domain extent and the temperature range (dashed areas) of the defects probed by SGMPCS, are indicated.

measurement conditions have to be carefully checked in order that the different used assumptions necessary to derive Eq. (40) can be fulfilled.

To be complete, we have also to note that there is a second order experimental feature that is not reproduced with the simulation. Indeed, if one compares carefully the temperature dependence of the relative experimental and simulated photocurrent maxima [Figs. 5 and 8(a), respectively], we can see that the maxima of the simulated curves exhibit a slight increase with temperature which is not observed experimentally. This could be due to a slight temperature dependence of different parameters that have not been taken into account in the present work, such as the optical or thermal capture cross sections, or the band gap energy. Which precise mechanism could be the predominant one was not the purpose of the present work and deserves further investigation.

In the following, we will discuss now more quantitatively some assumptions taken into account in this work, in order to allow simplified analytical relations between the imaginary part of the ac photocurrent and the DOS, given in Eq. (40). The following discussions are made in the framework of CIGS based heterojunctions, with typical values of CIGS physical parameters.

In order to discuss the assumption consisting to neglect dc optical transitions following Eq. (21), we have plotted in Fig. 9 the energy positions versus temperature of the level E_{ϕ_n} introduced by the same equation, for donorlike defects, and its equivalent one corresponding to acceptorlike defects, E_{ϕ_p}, in the case of CIGS as an illustration. These calculations have been done using Eq. (9) with the CIGS standard values of extended states effective densities, thermal capture cross sections and thermal velocities of electrons and holes, given at 300 K in Ref. 19. The temperature dependence of these parameters has been taken into account. For this calculation, we have taken 10^{-13} cm^2 for optical cross sections σ^{Opt} and 2×10^{12} ph cm^{-2} s^{-1} for the dc photon flux. In the same figure are indicated the peak energy positions of the shallow defect and the deepest one probed by SGMPCS, their energy domain extent and indications on the corresponding measurement temperature as it is derived from Fig. 7(c). We note that, for a probed donorlike (respectively, acceptorlike) defect of energy level E, we always have $E_C-E_{\phi_n}>E_C-E$ (respectively, $E_{\phi_n}-E_V>E-E_V$), and then $e_n(E)\gg e_n(E_{\phi_n})=\sigma_C^{Opt}\phi_{dc}+\sigma_V^{Opt}\phi_{dc}$ (respectively, $e_p(E)\gg e_p(E_{\phi_n})=\sigma_C^{Opt}\phi_{dc}+\sigma_V^{Opt}\phi_{dc}$) which allows the approximation following Eq. (21) where dc optical transitions were neglected against thermal emission frequencies.

The simplified expressions of ac electrons and holes photocurrent given in Eqs. (36) and (37), respectively, have been obtained assuming very small electrons and holes mean transit times compared to the modulation period. Assuming an electron mobility of about 100 cm^2 V^{-1} s^{-1}, and a hole mobility of about 25 cm^2 V^{-1} s^{-1} for CIGS,[19] a CIGS thickness of about 2 μm and an electric field of at least 10^4 V cm^{-1} (this electric field value is easily achievable in case of a 1 V reverse biased heterojunction), the transit time is of about 2×10^{-10} s for electrons and 8×10^{-10} s for holes. These values are much lower than the lowest light modulation period. Indeed, for a maximum value of our experimental modulation frequency, (i.e., 12 kHz), the corresponding period is 8.33×10^{-5} s, so that, approximations leading to Eqs. (36) and (37) are justified under these experimental conditions in case of CIGS based heterojunctions.

Additionally, since the ac photocurrent results from thermal and optical processes within the whole heterojunction, one wonders where is the precise spatial location of the responding defects to the subgap excitation. To answer this in the case of CIGS based solar cells, we have to compare the photon energy of the light excitation, $h\nu$, (about 0.95 ± 0.02 eV in our experimental setup) and the band gap values E_g of all the layers which are typically around 1.04 eV in our case for the absorber, (i.e., CIGS), 2.45 eV for the buffer layer (i.e., CdS) and 3.39 eV for the window layer (i.e., ZnO). For instance, an empty donorlike (respectively, acceptorlike) defect in the upper (respectively, lower) half of the band gap, situated at energy E_D (respectively, E_A), from the conduction (respectively, Valence) band edge, filled (respectively, emptied) with an optical transition from (respectively, to) the valence (respectively, conduction) band, with photon energy $h\nu$, can be probed by emitting thermally an electron (respectively, a hole) to the conduction (respectively, valence) band, only in the layer with a gap E_g such that:

$$E_g - h\nu < E_a, \tag{51}$$

where E_a is equal to E_C-E_D (respectively, E_A-E_V).

In our studies of CIGS based solar cells with SGMPCS, we were always in the case where

$$E_{g_{CIGS}} - h\nu < E_a < E_{g_{CdS}} - h\nu < E_{g_{ZnO}} - h\nu, \tag{52}$$

so that the probed defect is only located within the layer of the lowest band gap value (i.e., CIGS).

Furthermore, correlation between SGMPCS and AS, may result in an estimation of the optical cross section σ^{Opt} of the $\sigma^{Opt}\times N$ product if the corresponding defect is also probed by AS and presents the same physical parameters such as its thermal capture cross section and its energetic position within the band gap. This is what we have shown by applying successfully the SGMPCS technique to study the

DOS distribution in the band gap of the absorber layer of CIGS based solar cells.[13] We have found around 2.8×10^{-14} cm^2 for the optical cross section. We note that this value may depend on the precise nature of the CIGS compound. Indeed, several solar cells of different CIGS with varying stoichiometric composition, originating from different deposition processes, that we have investigated both by AS and SGMPCS, exhibit an optical cross section ranging from 3×10^{-14} to 1×10^{-12} cm^2. It is why in the present work, we have used 5×10^{-13} cm^2 as a mean order of magnitude for this optical cross section. In addition, note that the precision of this optical cross section determination also depends on the precision of the DOS value deduced from AS.

IV. CONCLUSION

A simple and powerful analysis of subgap modulated photocurrent is presented in the case of monovalent states. It allows the determination of the $\sigma^{Opt}\times N$ product distribution in the band gap of the absorber layer of n^+/p or p^+/n homojunction or heterojunction. We have shown in this work that when the technique is applied by carefully checking adequate experimental conditions (i.e., temperature and frequency ranges, subgap photon energy, dc and ac photon fluxes magnitude, and applied bias voltage), a simple formula relates directly the imaginary part of the experimental photocurrent to the DOS distribution and the corresponding thermal emission frequency. This technique can allow the DOS spectroscopy of more than one electrically active defect distribution if any. Indeed, results of our simulations with both one and two distinct defect distributions, compared to our experimental results, show the ability of the technique to reproduce the main evolutions with temperature and frequency of the experimental photocurrent and to derive the defects thermal emissions parameters. However, the use of the SGMPCS technique alone cannot allow one to distinguish between donorlike or acceptorlike defects. As the excitation process is different from those used in other defect spectroscopy techniques, such as AS or deep level transient spectroscopies, cross-checking their results will be useful to gain more information on the defect properties, especially in the case of disordered or partially crystallized semiconductors for which the results interpretations are not always straightforward. Depending on the semiconductor layer under investigation, further information could also be gained from the comparison of the experimental and simulated photocurrent of our model, to check if effects that have been neglected in this work, such as temperature or energetic position in the gap dependencies of thermal or optical capture cross sections for instance, are predominant effects to take into account or not.

TABLE III. Thermal emission and capture frequencies comparisons with their energetic and spatial validity domains.

Thermal frequencies comparison	Energetic domain	Spatial domain
$e_n(E)\gg c_n n(x)$	$E(x)>E_{f_n}$	$x>a$
$e_p(E)\gg c_p p(x)$	$E(x)<E_{f_p}$	$x<e$
$e_n(E)\gg c_p p(x)$	$\frac{E(x)+E_{f_p}}{2}>E_{mg}(x)$	$x<d$
$e_p(E)\gg c_n n(x)$	$\frac{E(x)+E_{f_n}}{2}<E_{mg}(x)$	$x>b$
$c_n n(x)\gg c_p p(x)$	$\frac{E_{f_n}+E_{f_p}}{2}>E_{mg}(x)$	$x<c$

ACKNOWLEDGMENTS

This work is partially supported by the Agence Nationale de la Recherche (ANR) BBCIGSE ANR-06-PSPV-002 project. The authors gratefully acknowledge F. Couzinié-Devy, N. Barreau, and J. Kessler for providing the samples.

APPENDIX

In order to simplify the steady state occupation function given by Eq. (10), we have to compare the thermal emission and capture frequencies one with each other. To do this, every thermal frequency has to be linked to one of the three others

$$e_n(E)=\exp\left[-\frac{2(E_{mg}-E)}{k_BT}\right]e_p(E), \tag{A1}$$

$$e_n=c_n n(x)\exp\left[\frac{E(x)-E_{f_n}(x)}{k_BT}\right], \tag{A2}$$

$$e_n=c_p p(x)\exp\left[\frac{E(x)+E_{f_p}(x)-2E_{mg}(x)}{k_BT}\right], \tag{A3}$$

$$e_p=c_p p(x)\exp\left[\frac{E_{f_p}(x)-E(x)}{k_BT}\right], \tag{A4}$$

$$e_p=c_n n(x)\exp\left[\frac{2E_{mg}(x)-E_{f_n}(x)-E(x)}{k_BT}\right], \tag{A5}$$

$$c_n n(x)=c_p p(x)\exp\left[\frac{E_{f_n}(x)+E_{f_p}(x)-2E_{mg}(x)}{k_BT}\right]. \tag{A6}$$

These equations led us to define five new abscissas (a, b, c, d, and e), as follows:

$$c_n n(a)=e_n(E), \tag{A7}$$

TABLE IV. Spatial ordering positions of the particular abscissa defined in Eqs. (A7)–(A11).

$E_0>E_{mg_0}$		$E_0<E_{mg_0}$	
$\frac{E_{f_p}-E_{f_n}}{2}>E-E_{mg}$	$\frac{E_{f_p}-E_{f_n}}{2}<E-E_{mg}$	$\frac{E_{f_n}-E_{f_p}}{2}>E-E_{mg}$	$\frac{E_{f_n}-E_{f_p}}{2}<E-E_{mg}$
$a<b<c<e<d$	$a<e<c<b<d$	$b<d<c<a<e$	$b<a<c<d<e$

TABLE V. Results of the thermal frequencies comparison within the three spatial subregions, in the upper, and the lower half of the band gap. The corresponding simplified dc occupation function is given for the six cases (i.e., three spatial subregions × two energetic subregions). We consider for this, that the quasi-Fermi level for electrons is always lower than the midgap level and that the quasi-Fermi level for holes is always higher than the midgap in the central subregion (cf. Fig. 3).

Spatial regions	$E_0 > E_{mg_0}:(e_n \gg e_p)$	$E_0 < E_{mg_0}:(e_n \ll e_p)$
$0<x<x_n$	$e_p \ll c_n n_{dc};\ c_p p_{dc} \ll c_n n_{dc};\ c_p p_{dc} \ll e_n;\ c_p p_{dc} \ll e_p$	$c_p p_{dc} \ll e_p$
	$f_{dc} = \dfrac{c_n n_{dc} + \sigma_V^{Opt}\phi_{dc}}{c_n n_{dc} + e_n + \sigma_V^{Opt}\phi_{dc} + \sigma_C^{Opt}\phi_{dc}}$	$f_{dc} = \dfrac{c_n n_{dc} + e_p + \sigma_V^{Opt}\phi_{dc}}{c_n n_{dc} + e_p + \sigma_V^{Opt}\phi_{dc} + \sigma_C^{Opt}\phi_{dc}}$
$x_n<x<x_p$	$c_p p_{dc} \ll e_n;\ E > E_{f_n} \Rightarrow c_n n_{dc} \ll e_n$	$c_n n_{dc} \ll e_p;\ E < E_{f_p} \Rightarrow c_p p_{dc} \ll e_p$
	$f_{dc} = \dfrac{\sigma_V^{Opt}\phi_{dc}}{e_n + \sigma_V^{Opt}\phi_{dc} + \sigma_C^{Opt}\phi_{dc}}$	$f_{dc} = \dfrac{e_p + \sigma_V^{Opt}\phi_{dc}}{e_p + \sigma_V^{Opt}\phi_{dc} + \sigma_C^{Opt}\phi_{dc}}$
$x>x_p$	$c_n n_{dc} \ll e_n$	$c_n n_{dc} \ll e_n;\ c_n n_{dc} \ll e_p;\ c_n n_{dc} \ll c_p p_{dc};\ e_n \ll c_p p_{dc}$
	$f_{dc} = \dfrac{\sigma_V^{Opt}\phi_{dc}}{e_n + c_p p_{dc} + \sigma_V^{Opt}\phi_{dc} + \sigma_C^{Opt}\phi_{dc}}$	$f_{dc} = \dfrac{e_p + \sigma_V^{Opt}\phi_{dc}}{c_p p_{dc} + e_p + \sigma_V^{Opt}\phi_{dc} + \sigma_C^{Opt}\phi_{dc}}$

$$c_n n(b) = e_p(E), \tag{A8}$$

$$c_n n(c) = c_p p(c), \tag{A9}$$

$$c_p p(d) = e_n(E), \tag{A10}$$

$$c_p p(e) = e_p(E). \tag{A11}$$

Resulting from the above thermal frequencies comparison, every abscissa is linked to a specific energy level as follows:

$$E(a) = E_{f_n}, \tag{A12}$$

$$E_{mg}(b) = \frac{E(b) + E_{f_n}}{2}, \tag{A13}$$

$$E_{mg}(c) = \frac{E_{f_p} + E_{f_n}}{2}, \tag{A14}$$

$$E_{mg}(d) = \frac{E(d) + E_{f_p}}{2}, \tag{A15}$$

$$E(e) = E_{f_p}. \tag{A16}$$

All the above equations allow us to compare thermal frequencies with each other in the energetic and the spatial domains as indicated in Table III. The different abscissa can be ordered, depending on the relations between the energetic levels, as shown in Table IV.

We have compared all thermal frequencies and we are able to know in which conditions they can be neglected. Furthermore, we can simplify the steady state occupation function in the three subregions delimited by x_n and x_p defined above, depending on the trap position and energetic level, as it is shown in Table V. Note that x_n is a particular a abscissa where $E_{mg}(x_n)=E_{f_n}$ and x_p is a particular e abscissa where $E_{mg}(x_p)=E_{f_p}$.

[1] C. Longeaud, J. A. Schmidt, and J. P. Kleider, Phys. Rev. B **73**, 235316 (2006).
[2] E. A. Niekisch, Ann. Phys. **450**, 279 (1955).
[3] H. Oheda, J. Appl. Phys. **52**, 6693 (1981).
[4] C. Longeaud, J. A. Schmidt, and R. R. Koropecki, Phys. Rev. B **73**, 235317 (2006).
[5] K. Hattori, Y. Musa, N. Murakami, N. Deguchi, and H. Okamoto, J. Appl. Phys. **94**, 5071 (2003).
[6] R. Herberholz, T. Walter, and H. W. Schock, J. Appl. Phys. **76**, 2904 (1994).
[7] G. Schumm and G. H. Bauer, Phys. Rev. B **39**, 5311 (1989).
[8] K. Abe, H. Okamoto, Y. Nitta, Y. Tsutsumi, K. Hattori, and Y. Hamakawa, Philos. Mag. B **58**, 171 (1988).
[9] D. Mencaraglia, Z. Djebbour, J. Sib, and S. Assal, J. Non-Cryst. Solids **164–166**, 247 (1993).
[10] J. D. Cohen and F. Zhong, J. Non-Cryst. Solids **190**, 123 (1995).
[11] P. Grygiel and W. Tomaszewicz, J. Phys.: Condens. Matter **12**, 5209 (2000).
[12] H. Okamoto and Y. Hamakawa, Solid State Commun. **24**, 23 (1977).
[13] J. Serhan, Z. Djebbour, A. Migan-Dubois, A. Darga, D. Mencaraglia, N. Barreau, J. Kessler, N. Naghavi, D. Lincot, and J. F. Guillemoles, Thin Solid Films **517**, 2256 (2009).
[14] M. Schmeits, M. Sakhaf, and S. Munnix, J. Appl. Phys. **74**, 6266 (1993).
[15] C. Longeaud, G. Fournet, and R. Vanderhaghen, Phys. Rev. B **38**, 7493 (1988).
[16] C. Longeaud and J. P. Kleider, Phys. Rev. B **45**, 11672 (1992).
[17] F. Couzinié-Devy, N. Barreau, and J. Kessler, Thin Solid Films **517**, 2407 (2009).
[18] T. Walter, R. Herberholz, C. Müler, and H. W. Schock, J. Appl. Phys. **80**, 4411 (1996).
[19] M. Gloeckler, A. L. Fahrenbruch, and J. R. Sites, Proceedings of the Third World Conference PVSEC, Osaka, Japan, 11–18 May 2003, p. 491.